A nonlocal elasticity theory to model the static behaviour of edge-cracked nanobeams

Daniela Scorza, Andrea Carpinteri, Camilla Ronchei, Andrea Zanichelli, Sabrina Vantadori
University of Parma, Italy
daniela.scorza@unipr.it, https://orcid.org/0000-0002-7376-4699
andrea.carpinteri@unipr.it, https://orcid.org/0000-0002-8489-6005
camilla.romchei@unipr.it, https://orcid.org/0000-0001-5450-4448
andrea.zanichelli@unipr.it, https://orcid.org/0000-0003-4152-8998
sabrina.vantadori@unipr.it, https://orcid.org/0000-0002-1904-9301

Raimondo Luciano
University of Naples Parthenope, Italy
raimondo.luciano@uniparthenope.it

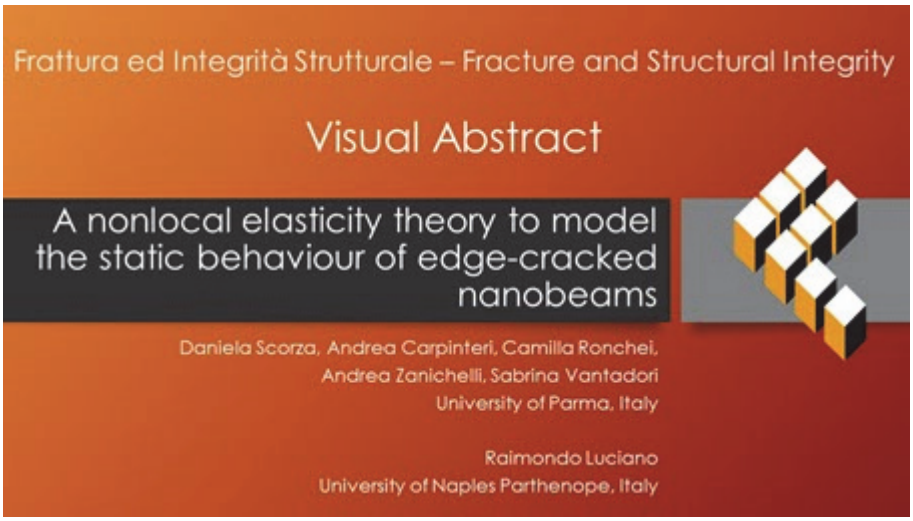

Citation: Scorza, D., Carpinteri, A., Ronchei, C., Zanichelli, A., Vantadori, S., Luciano, R., A nonlocal elasticity theory to model the static behaviour of edge-cracked nanobeams, Frattura ed Integrità Strutturale, 67 (2024) 280-291.

Received: 02.11.2023
Accepted: 23.11.2023
Online first: 09.12.2023
Published: 01.01.2024

KEYWORDS. Crack, Mixed-Mode loading, Nanobeam, Stress-Driven Model, Stress-Intensity Factor.

INTRODUCTION

Nanostructures are objects that range between 1nm and 100nm in at least one dimension. A zero-dimensional (0D) nanostructure has a nanometer scale in each direction of the three axes of an orthogonal reference frame (examples include nanoparticles, quantum dots and nanodots); a one-dimensional (1D) nanostructure has a nanometer scale

only in two directions (examples include nanowires, nanotubes, nanorods and nanobeams); a two-dimensional (2D) nanostructure has a nanometer scale only in one direction (examples include nanofilms, nanolayers and nanocoatings).
Although nanostructures have the same composition as the known materials in the bulk form, they generally have different physical, chemical and mechanical properties. Such properties change as their dimensions approach the atomic scale (that is, 1nm, being the atomic scale characterized by dimensions lower than 1nm). This is due to the surface area to volume ratio increase, resulting in material surface atoms dominating the material performance.
These nanostructures find application in new devices required by emerging research fields of nanotechnology, since nanostructures inside nanodevices are essential to their operations [1]. Examples are: nanoenergy, harvests nanomechanical resonators, nanoscale mass sensors, biological tissues, and electromechanical nanoactuators [2].
Moreover, nanostructures find application in composite materials, where one or more phases, having a nanometer scale, are embedded in a matrix. In terms of their matrix, nanocomposites are generally classified as [3]: ceramic-matrix [4-12], metal-matrix [13-21] and polymer-matrix nanocomposites [22-28]. More recently, research on cement-based materials (including concrete, mortar and cement paste) [29-35] has been trying to exploit the synergies that nanostructures can provide in terms of both improvement of their performance and acquisition of "smart" functions, making cement-based products become electric/thermal sensors or crack repairing materials [36].
In such a scenario, by focusing the attention on 1D nanostructures and more precisely on nanobeams, it is worth noticing that size-dependent continuum mechanics theories (named Generalised Continuum Theories, GCTs) have been proposed to explain the aforementioned size-dependent mechanical behaviour. Among them, the Stress-Driven nonlocal Model (SDM) has been recently employed to solve different engineering problems related to nanobeams without cracks, such as: static response [37,38], dynamic response [39-43], and buckling [44].
However, during thinning and machining processes of nanostructures, cracks are easily induced on their surface, becoming one of the failure sources when external forces are applied [45].
Therefore, in the present paper, the mechanical behaviour of edge-cracked nanobeams under Mixed-Mode loading is analytically investigated by exploiting the aforementioned SDM within the Euler-Bernoulli beam theory. In particular, according to the proposed formulation [46], the nanobeam is divided into two beam segments, linked through a massless spring at the cracked cross-section. The spring stiffness is computed by employing firstly the Griffith energy criterion, and then the conventional Linear Elastic Fracture Mechanics (LEFM), as long as the crack length is assumed to be greater than a critical crack size, so ensuring that LEFM does not breakdown. The transverse displacement is computed by exploiting the SDM for each beam segment. The formulation is then applied to simulate some experimental tests available in the literature [47-49].
The paper is organized as follows. In Section 2, the proposed formulation is outlined, whereas such a formulation is applied to a cantilever nanobeam in Section 3 and a parametric study is performed. In Section 4, the accuracy of the formulation is proved by comparing the analytical results with some data available in the literature. The main conclusions are summarized in Section 5.

FORMULATION FOR EDGE-CRACKED NANOBEAMS

Let us consider the edge-cracked nanobeam shown in Fig. 1(a), characterized by length L, thickness B, height H, with a crack of length a, whose center is located at a distance L_1 from the left-hand side of the nanobeam. The crack orientation is defined by the angle θ, measured with respect to the direction perpendicular to the beam axis.
The cracked nanobeam is modelled by two beam segments, linked through a massless elastic rotational spring with a stiffness k (Fig. 1(b)).
According to the SDM and under the Euler-Bernoulli hypothesis, the transverse displacement due to loads acting perpendicular to the beam axis can be determined by the following two equations [46] together with two constitutive boundary conditions and six continuity conditions:

$$v_1^{(6)}(x)-\frac{1}{L_c^2}v_1^{(4)}(x)=-\frac{1}{L_c^2}\frac{M_1^{(2)}(x)}{IE} \qquad 0\le x\le L_1 \tag{1}$$

$$v_2^{(6)}(x)-\frac{1}{L_c^2}v_2^{(4)}(x)=-\frac{1}{L_c^2}\frac{M_2^{(2)}(x)}{IE} \qquad L_1<x\le L \tag{2}$$

$$v_1^{(3)}(0)-\frac{1}{L_c}v_1^{(2)}(0)=0 \tag{3}$$

$$v_2^{(3)}(L)+\frac{1}{L_c}v_2^{(2)}(L)=0 \tag{4}$$

$$v_1^{(3)}(L_1)+\frac{1}{L_c}v_1^{(2)}(L_1)=\frac{2}{L_c}\chi_{1,2}(L_1) \quad \text{with} \quad \chi_{1,2}(x)=\int_{L_1}^{L}\Psi(x-t,L_c)\frac{M_2(t)}{IE}dt \tag{5}$$

$$v_2^{(3)}(L_1)-\frac{1}{L_c}v_2^{(2)}(L_1)=-\frac{2}{L_c}\chi_{2,1}(L_1) \quad \text{with} \quad \chi_{2,1}(x)=\int_{0}^{L_1}\Psi(t-x,L_c)\frac{M_1(t)}{IE}dt \tag{6}$$

$$v_1(L_1)=v_2(L_1) \tag{7}$$

$$v_2^{(1)}(L_1)-v_1^{(1)}(L_1)=\left[v_1^{(2)}(L_1)-L_c^2v_1^{(4)}(L_1)\right]\frac{IE}{k}=\frac{M_1(L_1)}{k} \tag{8}$$

$$v_1^{(4)}(L_1)-\frac{1}{L_c^2}v_1^{(2)}(L_1)=v_2^{(4)}(L_1)-\frac{1}{L_c^2}v_2^{(2)}(L_1) \tag{9}$$

$$v_1^{(5)}(L_1)-\frac{1}{L_c^2}v_1^{(3)}(L_1)=v_2^{(5)}(L_1)-\frac{1}{L_c^2}v_2^{(3)}(L_1) \tag{10}$$

where v_1 and v_2 are the transverse displacements of the left and right beam segments, respectively, I is the moment of inertia, E is the elastic modulus, M_1 and M_2 are the bending moments related to the left and right beam segments, respectively, and L_c is the material internal characteristic length ($0.0<\lambda=L_c/L\leq 1.0$).

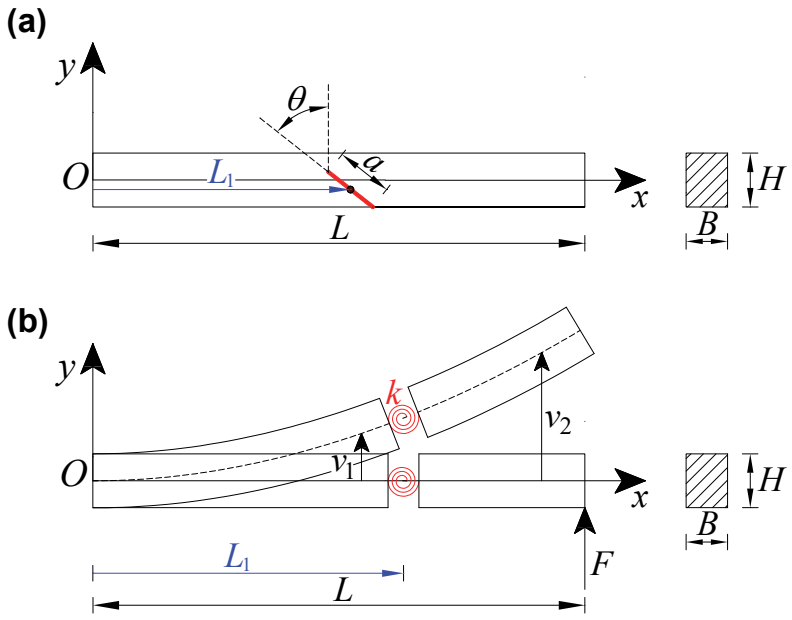

Figure 1: Edge-cracked nanobeam: (a) undeformed configuration and (b) schematisation according to the present formulation, both in the undeformed and in the deformed configuration.

Ψ is the averaging special kernel, computed as follows:

$$\Psi\left(x,L_c\right)=\frac{1}{2L_c}\exp\left(-\frac{|x|}{L_c}\right) \tag{11}$$

Note that further four boundary conditions at the beam ends are required to obtain a unique solution of the above elastic problem. In particular, for the case of a cantilever nanobeam with the free end in correspondence of $x=L$, such four boundary conditions are given by:

$$v_1\left(0\right)=0 \tag{12}$$

$$v_1^{(1)}\left(0\right)=0 \tag{13}$$

$$v_2^{(4)}\left(L\right)-\frac{1}{L_c^2}v_2^{(2)}\left(L\right)=0 \tag{14}$$

$$v_2^{(5)}\left(L\right)-\frac{1}{L_c^2}v_2^{(3)}\left(L\right)=\frac{1}{L_c^2}\frac{F}{IE} \tag{15}$$

being F the force applied at the free end, acting along the y-axis (see Fig. 1(b)).
The spring stiffness is computed by firstly exploiting the Griffith energy criterion, so that the compliance of a cracked plate under bending is derived as a function of the energy release rate, G. Then, the conventional LEFM is applied in order to express G as a function of the stress-intensity factors, K_I and K_{II}. It is worth noticing that such an approach is valid as long as the crack length is greater than a critical crack size. An example of the calculation of such a size is reported in Ref. [46], related to a single crystal of a silicon diamond-cubic structure, by obtaining a value of 15nm. For crack lengths greater than such a value, the LEFM continuum assumption, which postulates the presence of a large number of atoms in the vicinity of the crack tip, is not violated.
Therefore, the spring stiffness is given by:

$$k=\frac{BH^2E}{72\pi\left(1-\nu^2\right)}\frac{1}{\left[F_I\left(\xi\right)+F_{II}\left(\xi\right)\right]} \tag{16}$$

being ν the Poisson ratio, $\xi=a/H$ the relative crack depth, and $F_I(\xi)$ and $F_{II}(\xi)$ the correction functions for a given crack orientation θ, given by:

$$F_I\left(\xi\right)=\int_0^\xi z\,f_I^2\left(z\right)\,dz \tag{17}$$

$$F_{II}\left(\xi\right)=\int_0^\xi z\,f_{II}^2\left(z\right)\,dz \tag{18}$$

The functions f_I and f_{II}, for a given crack orientation θ, can be numerically obtained or, alternatively, empirical relationships available in the literature can be exploited [50-52].
It was experimentally found that, even in the case of beams with a height of the order of microns, size effect could be observed [53,54]. More precisely, the bending rigidity significantly increased, with respect to the classical one, when the height was decreased towards values of the same order of magnitude of the material microstructural sizes.
Therefore, regardless of the cross-section sizes (that is, even in the case of B and H greater than 100nm, being such a limit set by the 1D nanostructure definition), the above formulation can be conveniently applied in order to take into account

the size-dependent behaviour of small-scale structures, which is strongly needed even more as the cross-section sizes approach the material microstructural ones.

THE CASE OF A CANTILEVER NANOBEAM: A PARAMETRIC STUDY

Let us consider a nanobeam made of an aluminium alloy with elastic modulus E=70GPa and Poisson ratio ν=0.33. The geometric parameters characterizing the nanobeam are: L/H=20 and $B=H/2$. More precisely, L is equal to 150μm and the internal characteristic length is assumed as L_c=15μm (being such a value consistent with the average grain size of an aluminium alloy); consequently, a value of λ= 0.1 is deduced. The applied load F is equal to 10μN. Although the critical crack size should be calculated for the examined material, it can be assumed a value equal to 15nm (that is, that obtained for silicon in Ref. [46]), having the aluminium a face-centered-cubic crystal structure with a lattice parameter equal to 0.40478nm versus a diamond-cubic crystal structure and a lattice parameter of 0.543nm of the silicon. Two orientations of the crack are alternatively considered, that is, θ=22°.5 and 45°, being the f_I and f_{II} functions (obtained from empirical relationships available in the literature [55]) plotted in Fig. 2 for such cases.

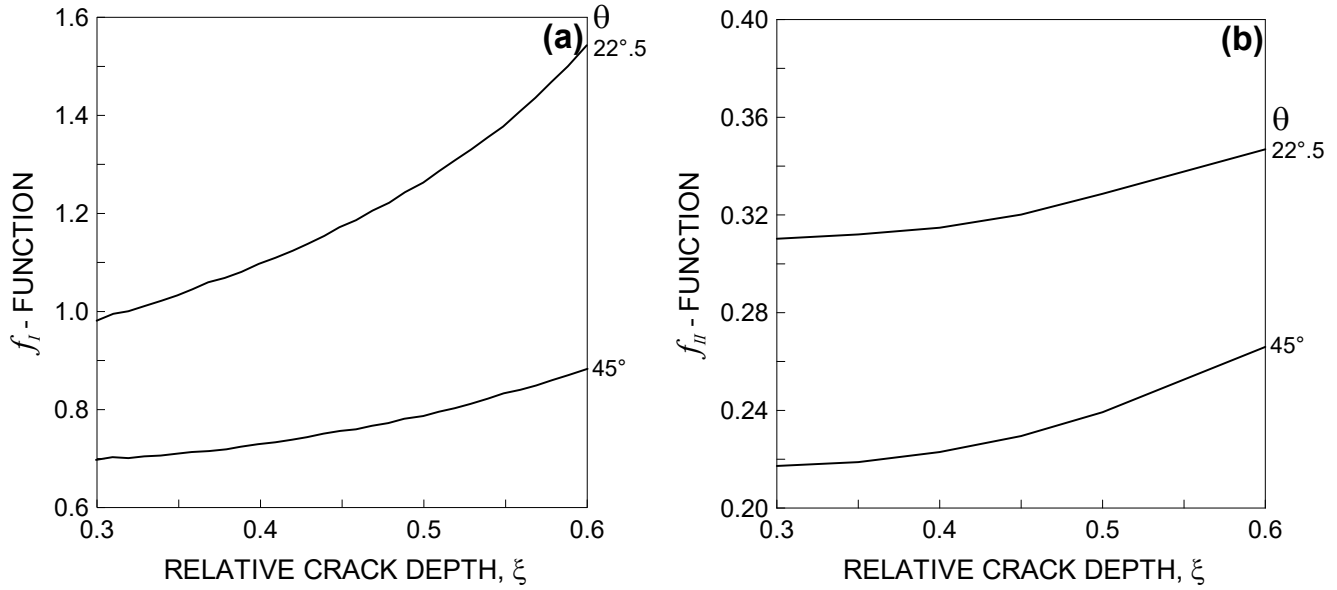

Figure 2: Functions: (a) f_I and (b) f_{II} for the crack orientation, θ, equal to 22°.5 and 45°.

By interpolating such curves with polynomials of fourth order, the functions reported in Tab. 1 are obtained. Moreover, the empirical function related to θ equal to 0° (taken from literature [56]) is also reported.

θ		INTERPOLATING FUNCTIONS	
0°		$1.122 - 1.40\xi + 7.33\xi^2 - 13.08\xi^3 + 14.0\xi^4$	$\xi \leq 0.6$
22°.5	f_I	$1.36638 - 5.57250\xi + 23.81393\xi^2 - 39.93405\xi^3 + 27.57030\xi^4$	$0.3 \leq \xi \leq 0.6$
45°		$0.88528 - 1.77873\xi + 5.51431\xi^2 - 6.80109\xi^3 + 4.23780\xi^4$	
22°.5	f_{II}	$0.19560 + 0.34145\xi - 1.77784\xi^2 + 3.52820\xi^3 - 1.97944\xi^4$	$0.3 \leq \xi \leq 0.6$
45°		$0.00569 + 3.09824\xi - 11.65355\xi^2 + 19.00464\xi^3 - 11.01432\xi^4$	

Table 1: f_I and f_{II} interpolating functions for the crack orientation, θ, equal to 0° [56], 22°.5 [55] and 45° [55].

Influence of ξ on transverse displacement

Let us consider a crack at the centre of the nanobeam, that is, $\eta=L_1/L=0.5$. Three values of ξ, that is, 0.3, 0.5 and 0.6, are examined.

The results in terms of transverse displacement are reported in Fig. 3(a) for $\theta=22°.5$ and in Fig. 3(b) for $\theta=45°$. Moreover, the results determined by applying the local beam theory (that is, $\lambda=0.0$) are also reported.

It can be observed that the transverse displacements computed according to the nonlocal theory are smaller than those obtained from the local one, independent of crack depth and crack orientation. More precisely, for $\theta=22°.5$ (Fig. 3(a)), the nonlocal values of v_2/H in correspondence of $x/L=1.0$ are about 14.30%, 13.44% and 12.63% smaller than the local ones, for ξ equal to 0.3, 0.5 and 0.6, respectively.

For $\theta=45°$(Fig. 3(b)), the displacement decreases become equal to about 14.46%, 14.01% and 13.64% for ξ equal to, respectively, 0.3, 0.5 and 0.6.

Moreover, for $\theta=22°.5$ (Fig. 3(a)), the nonlocal values of v_2/H in correspondence of $x/L=1.0$ increase of about 7.47% and 15,40% for ξ increasing from 0.3 to 0.5 and from 0.3 to 0.6, respectively, whereas such increments are equal to about 3.74% and 6.97% for $\theta=45°$ (Fig. 3(b)).

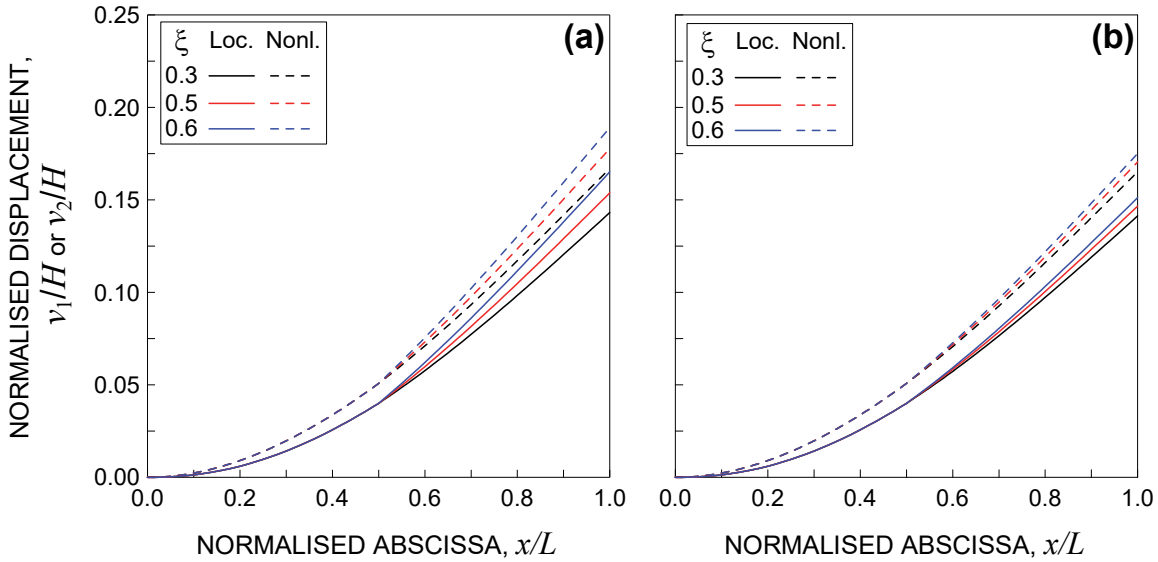

Figure 3: Normalised transverse displacement along the nanobeam axis for $\eta=0.5$ and θ equal to: (a) 22°.5 and (b) 45°, for different values of the relative crack depth ξ and according to both the nonlocal and the local beam theory.

Finally, by comparing Fig. 3(a) with Fig. 3(b), the nonlocal values of v_2/H in correspondence of $x/L=1.0$ decrease of about 1.26%, 4.69% and 8.47% for ξ equal to 0.3, 0.5 and 0.6, respectively, when the value of θ is made to vary from 22°.5 to 45°.

Influence of η on transverse displacement

Let us consider a crack characterized by a relative crack depth $\xi=0.5$. Three values of η, that is, 0.25, 0.50 and 0.75, are examined.

The results in terms of transverse displacement are reported in Fig. 4(a) for $\theta=22°.5$ and in Fig. 4(b) for $\theta=45°$. Moreover, the results for $\lambda=0.0$ are also reported.

It can be observed that the transverse displacements computed according to the nonlocal theory are smaller than those obtained from the local one, independent of the crack location and crack orientation. More precisely, for $\theta=22°.5$ (Fig. 4(a)), the nonlocal values of v_2/H in correspondence of $x/L=1.0$ are about 12.14%, 13.44% and 14.36% smaller than the local ones, for η equal to 0.25, 0.50 and 0.75, respectively. For $\theta=45°$(Fig. 4(b)), such displacement decreases become equal to about 13.23%, 14.01% and 14.52% for η equal to 0.25, 0.50 and 0.75, respectively.

Moreover, for θ=22°.5 (Fig. 4(a)), the nonlocal values of v_2/H in correspondence of x/L=1.0 decrease of about 11.01% and 17.62% for η increasing from 0.25 to 0.50 and from 0.25 to 0.75, respectively, whereas such increments are equal to about 6.40% and 10.23% for θ=45° (Fig. 4(b)).
Finally, by comparing Fig. 4(a) with Fig. 4(b), the nonlocal values of v_2/H in correspondence of x/L=1.0 decrease of about 9.40%, 4.69% and 1.27% for η equal to 0.25, 0.50 and 0.75, respectively, when the value of θ is made to vary from 22°.5 to 45°.

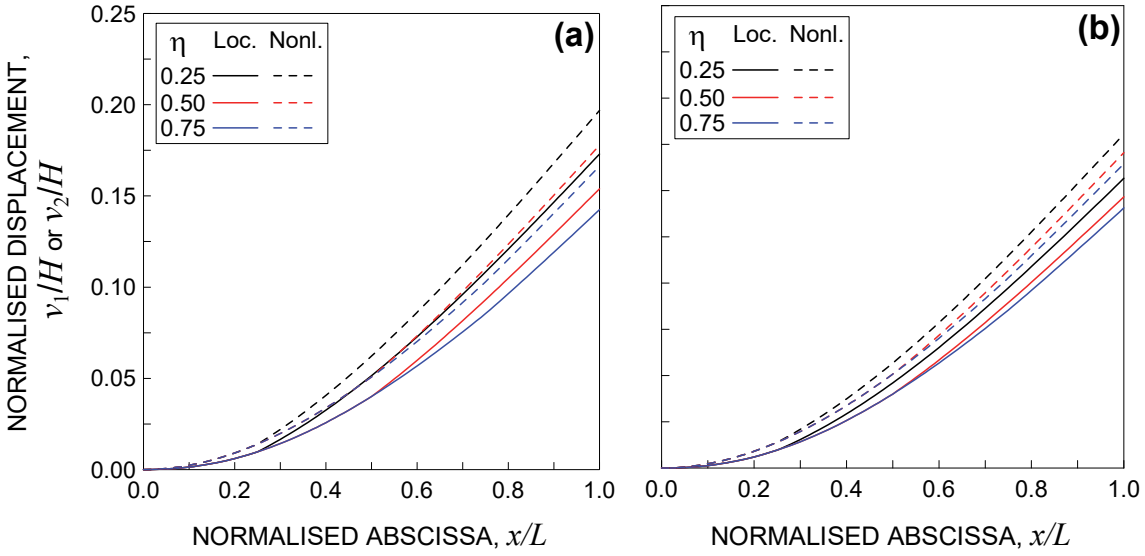

Figure 4: Normalised transverse displacement along the nanobeam axis for ξ=0.5 and θ equal to: (a) 22°.5 and (b) 45°, for different values of the relative crack location η and according to both the nonlocal and the local beam theory.

ACCURACY OF THE FORMULATION PROPOSED

In this Section, some experimental tests available in the literature [47-49], performed on both uncracked cantilever microbeams and cantilever microbeams containing a crack characterised by θ=0°, are analytically simulated. In particular, two aspects have to be pointed out:
- as far as the uncracked microbeams are concerned, the formulation presented in Ref. [46] is applied, since it represents a particular case of that here proposed;
- as far as the cracked microbeams are concerned, the formulation presented in Section 2 is applied, where f_{II}=0 (being the crack loaded under pure Mode I) and f_I is assumed to be equal to that reported in Tab. 1 for θ=0° [56].

Case study No.1

The tests reported in Ref. [47] are here briefly summarized. Each cantilever microbeam, with a rectangular cross-section, was fabricated by a standard photolithography process and a subsequent plasma etching. The microbeams were made of a (100) silicon wafer on which three different amorphous thin films (with increasing nitrogen content) were alternatively deposited, prior to lithography, by using the plasma enhanced chemical vapor deposition (PECVD) technique, and more precisely: a silicon oxide, a silicon oxynitride and a silicon nitride film. The specimen average sizes are listed in Tab. 2, where the beam axis was aligned to the [110] crystallographic direction of each (100) silicon wafer. For each specimen, a crack with the average length a listed in Tab. 2 was created via Focused Ion Beam (FIB) milling, perpendicular to the specimen axis, at a distance L_1 from the constrained end (see Tab. 2).
The bending tests were performed under load control at the rate of 1mNs^{-1}, by using a Hysitron Triloscope nanoindentation system, equipped by an atomic force microscope, at room temperature. The force was applied up to fracture failure. Nine specimens were tested.
The experimental results are shown in Fig. 5 in terms of scatter bands of the applied force against the deflection. It was observed that the behaviour was linear elastic up to failure, and that toughness increased by increasing the nitrogen content (that is, by moving from the silicon oxide scatter band to the silicon nitride one). In some cases, a horizontal pop-in was registered.

SPECIMEN FILM TYPE	$B\,[\mu m]$	$H\,[\mu m]$	$L\,[\mu m]$	$L_1\,[\mu m]$	$a\,[\mu m]$
Silicon oxide	1.69	2.10	7.15	2.00	0.36
Silicon oxynitride	1.66	2.10	6.95	1.85	0.38
Silicon nitride	1.57	2.10	6.74	1.84	0.32

Table 2: Case study No.1: average geometrical sizes of the tested specimens. Note that L represents the distance between the constrained end and the point where the force is applied.

For the analytical solutions, three notched beams with the sizes listed in Tab. 2 are considered. The elastic modulus is deduced from the force-deflection curves experimentally obtained from unnotched cantilever microbeams and proved in Ref. [47]. The elastic modulus E is equal to: 43GPa for the case of silicon oxide thin film, 52GPa for the case of silicon oxynitride thin film, and 105GPa for the case of silicon nitride thin film.

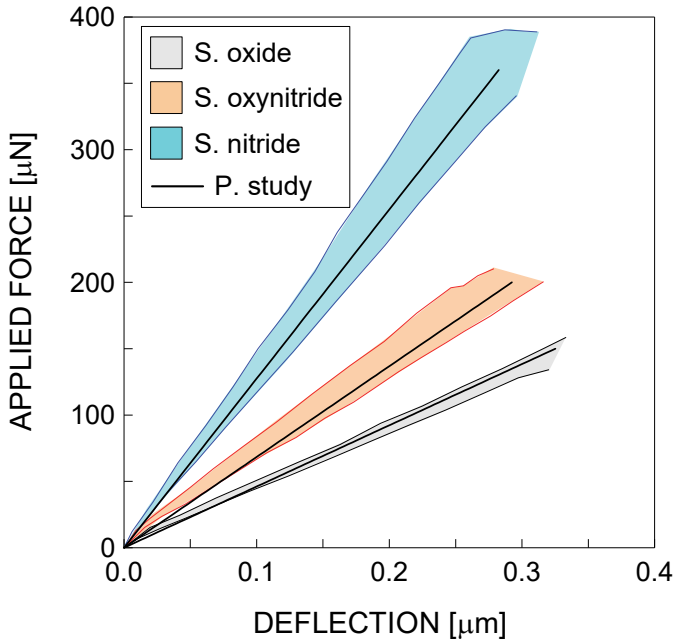

Figure 5: Case study No.1: applied force against deflection. Scatter bands of the experimental curves and analytical curves are plotted.

The Poisson ratio is assumed to be equal to 0.36 [57]. The dimensionless characteristic length is assumed to be equal to λ=0.08 (that is, L_c=0.55 μm), which is consistent with the grain size equal to 0.55μm reported in Ref. [58].
The analytical results are reported in Fig. 5. It can be observed that a satisfactory agreement is obtained, being the analytical curves perfectly inside the corresponding experimental scatter bands.

Case study No.2

The tests reported in Ref. [48] are here briefly summarized. Each cantilever microbeam, with a rectangular cross-section, was fabricated by micromachining and employing a FIB. The microbeams were extracted from a Si(100) wafer, with nominal sizes equal to 5μm(B)x5μm(H)x20μm(L), being L the distance between the constrained end and the point where the force is applied. A crack with a nominal length a of 2.3μm was milled, perpendicular to the beam axis (corresponding to the [010] crystallographic direction) and at a distance L_1=5.3μm from the constrained end. The bending tests were performed under displacement control at rate equal to about 5nms^{-1}, by using an ASMEC UNAT SEM-2 nanoindenter inside a SEM at room temperature. The force was applied up to fracture failure. Five specimens were tested.
The experimental results are shown in Fig. 6 in terms of scatter band of the applied force against the deflection. It was observed that the microbeams deform in an ideally elastic-brittle manner.
For the analytical solution, a notched beam with the experimental nominal sizes is considered. The elastic modulus is equal to E=169GPa [57], whereas the Poisson ratio is equal to ν=0.36 [57]. The dimensionless characteristic length is assumed to be equal to λ=0.03 (that is, L_c=0.55μm), which is consistent with the grain size equal to 0.55μm reported in Ref. [58].

The analytical results are reported in Fig. 6. It can be observed that a satisfactory agreement is obtained, being the analytical curve perfectly inside the experimental scatter band. Note that the analytical curve has been graphically translated on the right of about 17nm, since the initial part of the experimental scatter band is characterised by a non-linear behaviour due to the experimental setup.

Case study No.3

The tests reported in Ref. [49] are here briefly summarized. Each cantilever microbeam, with a rectangular cross-section, was fabricated by milling and employing a FIB. The microbeams were made by a FeAl single crystalline material with B2 ordered structure, with nominal sizes equal to 4μm(*B*)x2μm(*H*)x8μm(*L*). The bending tests were performed under displacement control at rate of 1nms^{-1}, by using a PI-85 Pico-indenter system inside an environmental SEM under vacuum. The force was applied up to a deflection of 5μm. Two specimens were tested.

The experimental results are shown in Fig. 7 in terms of the applied force against the deflection. It was observed that, from a given value of the deflection, the load is quite constant and no crack nucleation/propagation occurs.

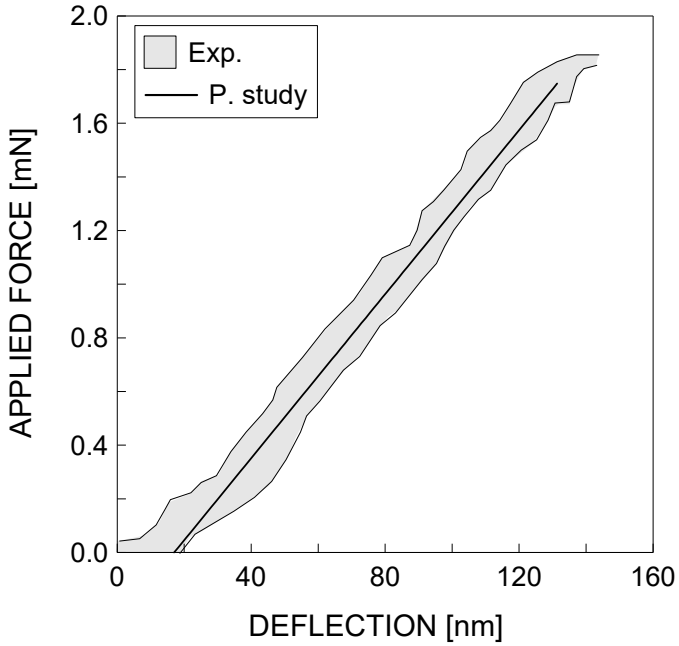

Figure 6: Case study No.2: applied force against deflection. Scatter band of the experimental curves and analytical curve are plotted.

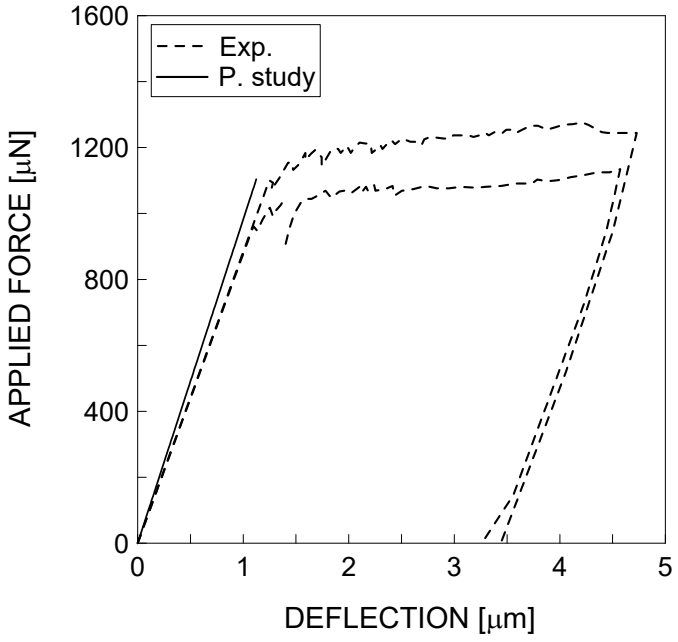

Figure 7: Case study No.3: applied force against deflection. Experimental curves and analytical curve are plotted.

For the analytical solution, a beam with the experimental nominal sizes is considered. The elastic modulus is equal to E=75.9GPa [59], whereas the Poisson ratio is equal to ν=0.30 [60]. The dimensionless characteristic length is assumed to be equal to λ=0.38, computed by considering an internal characteristic length L_c equal to the material grain size, that is, 3μm [61].

The analytical results are reported in Fig. 7. It is worth noting that only the elastic behaviour is simulated, the formulation presented in Ref. [46] being developed under the Euler-Bernoulli theory.

It can be observed that the slope of the elastic branch differs from the experimental one of about 11.93%, and that, at a load value equal to 960μN, the deflection differs of about -10.36% from the average experimental one.

Conclusions

The mechanical behaviour of an edge-cracked nanobeam under Mixed-Mode loading has been analytically examined. More precisely, the nanobeam has been divided into two beam segments linked through a massless spring at the cracked section. The stiffness of the spring has been computed according to both the Griffith criterion and concepts of the LEFM, being the length of the crack assumed greater than a critical crack size.

The proposed formulation has been applied to the case of a cantilever edge-cracked nanobeam, performing a parametric study to analyse the mechanical behaviour by varying the crack depth and the crack location along the beam axis.
Finally, the formulation has been applied to some experimental data available in the literature. It has been observed that:
(i) for the silicon materials analysed, a satisfactory agreement between experimental and analytical results has been obtained, being the numerical curves perfectly inside the experimental scatter bands;
(ii) for the FeAl single crystalline material, a maximum error on the deflection equal to about -10.36% is obtained with respect to the average experimental one, when the load is equal to 960μN.

Acknowledgements

The work of Camilla Ronchei, Sabrina Vantadori and Andrea Zanichelli is supported by Italian Ministry of University and Research (P.R.I.N. National Grant 2020, Project code 2020EBLPLS; University of Parma Research Unit).

References

[1] Ramsden, J.J. (2016). Nanotechnology: An Introduction, 2nd Edition, Elsevier, Amsterdam, UK.
[2] Chandel, V.S., Wang, G. and Talha, M. (2020). Advances in modelling and analysis of nano structures: A review, Nanotechnol. Rev., 9, pp. 230–258.
[3] Camargo, P.H.C., Satyanarayana, K.G. and Wypych, F. (2009). Nanocomposites: Synthesis, structure, properties and new application opportunities, Mater. Res., 12, pp. 1–39.
[4] Li, L. (2021). A micromechanical tension-tension fatigue hysteresis loops model of fiber-reinforced ceramic-matrix composites considering stochastic matrix fragmentation, Int. J. Fatigue, 143, art. no. 106001.
[5] Hou, G., Shang, D.G., Zuo, L.X., Qu, L.F., Xia, M., Wu, S. and Hao, G.C. (2022). Fatigue life prediction of needled ceramic matrix composite under variable amplitude loading, Int. J. Fatigue, 156, art. no. 106690.
[6] Xiang, W., Li, X., Ni, H. and Liu, B. (2022). Micromechanical analysis of fiber-reinforced ceramic matrix composites by a hierarchical quadrature element method, Compos. Struct., 300, art. no. 116143.
[7] Yu, G., Jia, Y., Xie, C., Du, J., Gao, X., Song, Y. and Wang, F. (2022) Transverse tensile mechanical experimental method and behavior of ceramic matrix mini-composites, Compos. Struct., 297, art. no. 115923.
[8] Zhao, C., Tu, Z., Mao, J., Chen, P. and Li, L. (2022). The design of special woven-preformed structures for the high-performance film cooling with undamaged fibers based on 2.5D ceramic matrix composites, Compos. Struct., 283, art. no. 115114.
[9] Reimer, T., Di Martino, G.D., Sciti, D., Zoli, L., Galizia, P., Vinci, A., Lagos, M.A. and Azurmendi, N. (2023). Experimental characterization of fatigue life of ZrB2-SiC based ultra high-temperature ceramic matrix composites, Int. J. Fatigue, 168, art. no. 107389.
[10] Wan, Y., Wang, R., Jia, B., Zhou, S., Liu, Y., Cai, H., Gu, M., Li, D. and Li, W. (2023). Characterization of temperature dependence of fracture behavior of monolithic and laminated ultra-high temperature ceramic matrix composites, Fatigue Fract Eng Mater Struct., 46, pp. 895–908.
[11] Yang, Z., Li, W., Chen, Y., Zeng, W., Chen, W. and Cao, X. (2023). Life assessment of thermomechanical fatigue in a woven SiC/SiC ceramic matrix composite with an environmental barrier coating at elevated temperature, Int. J. Fatigue, 172, art. no. 107584.
[12] Yao, L., Liu, Z., Song, Q., Wang, B. and Cai, Y. (2023). Prediction modelling of cutting force in rotary ultrasonic end grinding 2.5D woven SiO2f/SiO2 ceramic matrix composite, Compos. Struct., 304, art. no. 116448.
[13] Azadi, M. and Aroo, H. (2021). Bending cyclic behavior and scatter-band analysis of aluminum alloys under beneficial and detrimental conditions through high-cycle fatigue regime, Frattura ed Integrita Strutturale, 15, pp. 272–281.
[14] Basiri, A., Dadashi, A., Azadi, M., Winter, G., Seisenbacher, B. and Grün, F. (2021). Effect of nano-clay addition and heat treatment on tensile and stress-controlled low-cycle fatigue behaviors of aluminum-silicon alloy, Frattura ed Integrita Strutturale, 15, pp. 373–397.
[15] Ravikumar, M., Reddappa, H.N., Suresh, R., Babu, E.R. and Nagaraja, C.R. (2021). Study on micro-nano sized al2 o3 particles on mechanical, wear and fracture behavior of al7075 metal matrix composites, Frattura ed Integrita Strutturale, 15, pp. 166–178.

[16] Arun, J., Ansalam Raj, T.G., Reby Roy, K.E. and Suresh, S. (2022). Fatigue life, distortion behavior of AA 8011- nano B4C composite using simulated acoustic emission technique – An experimental and statistical appraisal, Int. J. Fatigue, 164, art. no. 107168.
[17] Bright, R.J. and Hariharasakthisudhan, P. (2022). Mechanical characterization and analysis of tensile fracture modes of ultrasonically stir cast Al6082 composites reinforced with Cu powder premixed Metakaolin particles, Frattura ed Integrita Strutturale, 16, pp. 426–438.
[18] Djellal, N., Mekki, D.E., Navarro, E. and Marin, P. (2022). Influence of Pr6O11 addition on structural and magnetic properties of mechanically alloyed Fe65Co35 nanoparticles, Frattura ed Integrita Strutturale, 16, pp. 396–406.
[19] Molaei, F., Hamed Mashhadzadeh, A., Spitas, C. and Reza Saeb, M. (2022). Atomistic analysis of 3D fracture fingerprints of mono- and bi-crystalline diamond and gold nanostructures, Eng. Fract. Mech., 263, art. no. 108291.
[20] Ravikumar, M. and Naik, R. (2022). Impact of nano sized SiC and Gr on mechanical properties of aerospace grade Al7075 composites, Frattura ed Integrita Strutturale, 16, pp. 439–447.
[21] Dai, Y., Li, Y., Zan, Z. and Qin, F. (2023). Bondline thickness effect on fracture and cohesive zone model of sintered nano silver adhesive joints under end notched flexure tests, Fatigue Fract Eng Mater Struct., 46(6), pp. 2062–2079.
[22] Joshi, A.G., Basavarajappa, S., Ellangovan, S. and Jayakumar, B.M. (2021). Investigation on influence of sicp on three-body abrasive wear behaviour of glass/epoxy composites, Frattura ed Integrita Strutturale, 15, pp. 65–73.
[23] Santos, P., Maceiras, A., Valvez, S. and Reis, P.N.B. (2021). Mechanical characterization of different epoxy resins enhanced with carbon nanofibers, Frattura ed Integrita Strutturale, 15, pp. 198–212.
[24] Khashaba, U.A. and Najjar, I.M.R. (2022). A new approach for fatigue damage detection in adhesive joints modified with nanoparticles under different temperatures, Fatigue Fract Eng Mater Struct., 45, 1763–1783.
[25] Rao, Y.S., Shivamurthy, B., Mohan, N.S. and Shetty, N. (2022). Influence of hBN and MoS2 fillers on toughness and thermal stability of carbon fabric-epoxy composites, Frattura ed Integrita Strutturale, 16, pp. 240–260.
[26] Wang, H. and Shin, H. (2022). Influence of nanoparticulate diameter on fracture toughness enhancement of polymer nanocomposites by an interfacial debonding mechanism: A multiscale study, Eng. Fract. Mech., 261, art. no. 108261.
[27] Tiwari, A. and Panda, S.K. (2023). Fracture energy of CNT/epoxy nanocomposites with progressive interphase debonding, cavitation, and plastic deformation of nanovoids, Fatigue Fract Eng Mater Struct., 46, pp. 1170–1189.
[28] Wang, H. and Shin, H. (2023). A multiscale model to predict fatigue crack growth behavior of carbon nanofiber/epoxy nanocomposites, Int. J. Fatigue, 168, art. no. 107467.
[29] Danoglidis, P.A., Gdoutos, E.E. and Konsta-Gdoutos, M.S. (2022). Designing carbon nanotube and nanofiber-polypropylene hybrid cementitious composites with improved pre- and post- crack load carrying and energy absorption capacity, Eng. Fract. Mech., 262, art. no. 108253.
[30] Li, Y., Li, L., Wan, D., Sha, A., Li, Y. and Liu, Z. (2022). Preparation and evaluation of a fluorinated nano-silica superhydrophobic coating for cement pavement, Constr. Build. Mater., 360, art. no. 129478.
[31] Li, L., Wang, X., Du, H. and Han, B. (2022). Comparison of compressive fatigue performance of cementitious composites with different types of carbon nanotube, Int. J. Fatigue, 165, art. no. 107178.
[32] Shilar, F.A., Ganachari, S.V. and Patil, V.B. (2022). Advancement of nano-based construction materials - A review, Constr. Build. Mater., 359, art. no. 129535.
[33] Singh, H., Kumar Tiwary, A. and Singh, S. (2023). Experimental investigation on the performance of ground granulated blast furnace slag and nano-silica blended concrete exposed to elevated temperature, Constr. Build. Mater., 394, art. no. 132088.
[34] Goyal, R., Verma, V.K. and Singh, N.B. (2023). Hydration of Portland slag cement in the presence of nano silica, Constr. Build. Mater., 394, art. no. 132173.
[35] Vantadori, S., Magnani, G., Mantovani, L., Pontiroli, D., Ronchei, C., Scorza, D., Sidoli, M., Zanichelli, A. and Riccò, M. (2022). Effect of GO nanosheets on microstructure, mechanical and fracture properties of cement composites, Constr. Build. Mater., 361, art. no.129368.
[36] Bastos, G., Patiño-Barbeito, F., Patiño-Cambeiro, F. and Armesto, J. (2016). Nano-inclusions applied in cement-matrix composites: A review, Materials, 9, art. no. 1015.
[37] Barretta, R., Marotti de Sciarra, F., Pinnola, F.P. and Vaccaro, M.S. (2022). On the nonlocal bending problem with fractional hereditariness, Meccanica, 57(4), pp. 807–820.
[38] Pinnola, F.P., Vaccaro, M.S., Barretta, R. and Marotti de Sciarra, F. (2022). Finite element method for stress-driven nonlocal beams, Eng. Anal. Bound. Elem., 134, pp. 22–34.
[39] Apuzzo, A., Bartolomeo, C., Luciano, R. and Scorza, D. (2020). Novel local/nonlocal formulation of the stress-driven model through closed form solution for higher vibrations modes, Compos. Struct., 252, art. no. 112688.

[40] Luciano, R., Darban, H., Bartolomeo, C., Fabbrocino, F. and Scorza, D. (2020). Free flexural vibrations of nanobeams with non-classical boundary conditions using stress-driven nonlocal model, Mech. Res. Commun., 107, art. no. 103536.
[41] Penna, R., Feo, L., Fortunato, A. and Luciano, R. (2021). Nonlinear free vibrations analysis of geometrically imperfect FG nano-beams based on stress-driven nonlocal elasticity with initial pretension force, Compos. Struct., 255, art. no. 112856.
[42] Pinnola, F.P., Vaccaro, M.S., Barretta, R. and Marotti de Sciarra, F. (2021). Random vibrations of stress-driven nonlocal beams with external damping, Meccanica, 56(6), pp. 1329–1344.
[43] Russillo, A.F., Failla, G., Alotta, G., Marotti de Sciarra, F. and Barretta, R. (2021). On the dynamics of nano-frames, Int. J. Eng. Sci., 160, art. no. 103433.
[44] Barretta, R., Fabbrocino, F., Luciano, R., de Sciarra, F.M. and Ruta, G. (2020). Buckling loads of nano-beams in stress-driven nonlocal elasticity, Mech. Adv. Mater. Struct., 27, pp. 869–875.
[45] Yeh, M.K., Shao, Y.K., Yeh, J.A. and Hsu C. (2017). Stress distribution affected by nanostructures near a surface crack on a silicon chip, Acta Mech., 228, pp. 2791–2797.
[46] Scorza, D., Luciano, R., Caporale, A. and Vantadori, S. (2023). Nonlocal analysis of edge-cracked nanobeams under Mode I and Mixed-Mode (I + II) static loading, Fatigue Fract Eng Mater Struct., 46, pp. 1426–1442.
[47] Matoy, K., Schönherr, H., Detzel, T., Schöberl, T., Pippan, R., Motz, C. and Dehm, G. (2009). A comparative micro-cantilever study of the mechanical behavior of silicon based passivation films, Thin Solid Films, 518, pp. 247–256.
[48] Jaya, B.N., Kirchlechner, C. and Dehm, G. (2015). Can microscale fracture tests provide reliable fracture toughness values? A case study in silicon, J. Mater. Res., 30, pp. 686–698.
[49] Deng, Y., Hajilou, T. and Barnoush, A. (2017). Hydrogen-enhanced cracking revealed by in situ micro-cantilever bending test inside environmental scanning electron microscope, Philos. Trans. Royal Soc. A, 375, 20170106.
[50] Tada, H., Paris, P. and Irwin, G. (1973). The Stress Analysis of Cracks Handbook, Del Research Corporation, Woodbourne, St. Louis, Missouri.
[51] Murakami, Y. (1987). Stress Intensity Factors Handbook, Volume 1, Pergamon.
[52] Murakami, Y. (1987). Stress Intensity Factors Handbook, Volume 2, Pergamon.
[53] Lam, D.C.C., Yang, F., Chong, A.C.M., Wang, J. and Tong, P. (2003). Experiments and theory in strain gradient elasticity, J. Mech. Phys. Solids, 51, pp. 1477–1508.
[54] Mcfarland, A.W. and Colton, J.S. (2005). Role of material microstructure in plate stiffness with relevance to microcantilever sensors. J. Micromech. Microeng., 15, pp. 1060–1067.
[55] Wilson, W.K., Clark, W.G. and Wessel, E.T. (1968). Fracture Mechanics Technology for combined loading and low to intermediate strength metals. Final Technical Report No. 10276, Westinghouse Research Laboratories.
[56] Gross, B. and Srawley, J.E. (1965). Stress-intensity factors for single-edge-notch specimens in bending or combined bending and tension by boundary collocation of a stress function NASA, Technical Note D-2603.
[57] Hopcroft, M.A., Nix, W.D. and Kenny, T.W. (2010). What is the Young's Modulus of Silicon? JMEMS, 19, pp. 229–238.
[58] Lee, J.N., Choi, Y.W., Lee, B.J. and Ahna, B.T. (1997). Microwave-induced low-temperature crystallization of amorphous silicon thin films, J. Appl. Phys., 82(6), pp. 2918–2921.
[59] Göken, M., Thome, F. and Vehoff, H. (2002). Study of crack tip deformation in FeAl and NiAl crystals with optical interference microscopy and atomic force microscopy, Philos. Mag. A, 82, pp. 3241–3250.
[60] Deng, Y. and Barnoush, A. (2018). Hydrogen embrittlement revealed via novel in situ fracture experiments using notched micro-cantilever specimens, Acta Mater., 142, pp. 236–247.
[61] Salazar, M., Albiter, A., Rosas, G. and Perez, R. (2003). Structural and mechanical properties of the AlFe intermetallic alloy with Li, Ce and Ni additions, Mater. Sci. Eng., A351, pp. 154–159.